High-performance phototransistors by alumina encapsulation of a two-dimensional semiconductor with self-aligned contacts

Guangda Liang, Yiming Wang, Jiawei Zhang, Zakhar R. Kudrynskyi, Zakhar Kovalyuk, Amalia Patanè, Qian Xin*, and Aimin Song**

G. D. Liang, Y. M. Wang, Prof. J. W. Zhang, Prof. Q. Xin, Prof. A. M. Song
Shandong Technology Center of Nanodevices and Integration
State Key Laboratory of Crystal Materials
School of Microelectronics
Shandong University
Jinan 250100, China
Email: xinq@sdu.edu.cn

Z. Kudrynskyi, Prof. A. Patanè
School of Physics and Astronomy
University of Nottingham
Nottingham NG7 2RD, UK
Email: Amalia.Patane@nottingham.ac.uk

Z. Kovalyuk
Frantsevich Institute for Problems of Materials Science
The National Academy of Sciences of Ukraine
Chernivtsi Branch, Chernivtsi 58001, Ukraine

Prof. Q. Xin
Shenzhen Research Institute of Shandong University
Shenzhen 518057, China

Prof. A. M. Song
Department of Electrical and Electronic Engineering
University of Manchester
Manchester M13 9PL, United Kingdom
Email: A.Song@manchester.ac.uk

Keywords: InSe, 2D material, encapsulation, photodetector, transistor

Abstract: Two-dimensional (2D) semiconductors are promising candidates for next generation electronics and optoelectronics. However, their exposure to air and/or resists during device fabrication can cause considerable degradation of material quality, hindering their study and exploitation. Here, field effect transistors (FETs) are designed and fabricated by encapsulation of the 2D semiconductor indium selenide (InSe) with alumina (Al_2O_3) and by self-aligned electrical contacts. The Al_2O_3-film is grown directly on InSe immediately after its exfoliation to provide a protecting capping layer during and after device fabrication. The InSe-FETs exhibit a high electron mobility of up to ~ 10^3 cm^2/Vs at room temperature for a 4-nm-thick InSe layer, a low contact resistance (down to 0.18 kΩ) and a high, fast, and broad-band photoresponsivity. The photoresponsivity depends on the InSe-layer thickness and photon wavelength, reaching a value of up to 10^8 A/W in the visible spectral range, one order of magnitude larger than previously reported for similar photodetectors. The proposed fabrication is scalable and suitable for high-precision pattern definition. It could be extended to other 2D materials and multi-layer structures where alumina could also provide effective screening of the electric field induced by polar molecules and/or charged impurities present near the surface of the 2D layer.

1. Introduction

Two-dimensional (2D) materials have attracted much attention because of their unique electronic properties and potential for applications in next generation electronic and optoelectronic devices.[1,2] In the past decade, different 2D layered materials have been explored, such as graphene,[1] transitional metal dichalcogenides (TMDs),[3,4] black phosphorus,[5] and III-VI group semiconductors.[6-8] However, the exposure to air and resists of some 2D materials during device fabrication can cause considerable degradation of material quality, hindering their study and exploitation. Amongst 2D semiconductors, indium selenide (InSe) is regarded as one of the most promising system for miniaturized electronics and optoelectronics due to its light electron effective mass ($0.14m_0$, m_0 is the free electron mass) and highly tunable band gap.[6] In particular, the electron mobility (μ) can reach values of up to 10^3 cm^2/Vs and 10^4 cm^2/Vs at room temperature and liquid helium temperature, respectively.[8] In recent years, different structures have been proposed and studied for improving the performance of devices based on InSe and its heterostructures.[9] For example, in 2014, Lei *et al.* reported an InSe-based photodetector with a responsivity R of 34.7 mA/W.[10] In 2018, Spencer *et al.* improved the responsivity to 10^7 A/W by decreasing the density of surface traps.[11] Mudd *et al.* also reported on graphene/InSe/graphene heterostructures with a responsivity of up to 10^5 A/W.[7]

Despite the improved performance over the last few years, robust and scalable processes for the fabrication of high-quality devices are still missing. Previous experiments suggest that thin exfoliated flakes of InSe tend to degrade in air due to interaction with chemical species, such as oxygen and water. For example, InSe flakes can show a significant decrease in photoluminescence (PL) intensity by about 80% after one month exposure to air.[8] Similarly,

the characteristic vibrational modes in the Raman spectrum can vanish over time, indicating that the lattice structure and its interaction with light can be altered by oxidation and/or adsorption of water molecules.[12] X-Ray photoelectron spectroscopy analysis suggests that the oxidation process can affect layers that are far from the surface.[13] In particular, in the presence of Se vacancies, InSe has a strong propensity to react with water and oxygen, resulting in deep level trap states.[14]

As for other 2D materials, InSe can be contaminated by photoresists used during fabrication. It is usually difficult to completely remove all the photoresist residues, which degrade device performance by decreasing carrier mobility and creating unwanted doping.[15,16] Water in the photoresist developer can further accelerate the degradation of the InSe flakes. Thus, most of the InSe field-effect transistors (FETs) fabricated using shadow masks have a mobility much higher than those fabricated by photolithography.[12,17,18] However, the shadow mask approach is not compatible with scalable manufacturing and cannot deliver high-precision pattern definition. To overcome this problem, polymethyl methacrylate (PMMA) has been used to protect InSe,[19-21] but the field effect mobility of InSe FETs fabricated by using electron-beam lithography (EBL) is still about one order of magnitude lower than that using shadow masks.[21-23] Thus, further research is required to develop micro/nano-fabrication processes of InSe for high-performance FETs, photodetectors, and high-speed electronics.[24-26]

Previous efforts to prevent the degradation of InSe in air include encapsulation with hexagonal boron nitride[8,27] and PMMA.[20] While encapsulation with exfoliated hexagonal boron nitride has yielded stable charge transport characteristics, this method possesses significant processing challenges, especially in terms of scalable manufacturing. PMMA

provides a good encapsulation of InSe and it has been used to modify the surface of semiconductors, resulting in improved device performance.[19,20] However, it can be dissolved in solvents and can introduce contamination during fabrication. On the other hand, alumina (Al_2O_3) is one of the most used high-*k* materials: it has a large bandgap (E_g ~8 eV), a high dielectric constant (~ 9.0), a high breakdown field (5–10 MV/cm), strong ability of adhesion to dissimilar materials, and superior thermal and chemical stability.[28] Previous work on thin Al_2O_3 films grown by atomic-layer deposition (ALD) has demonstrated excellent properties with leakage currents below 10^{-8}A/cm^2, which is one of the lowest amongst high-*k* dielectrics.[29,30] It has been reported previously that Al_2O_3 encapsulation provides an effective way to protect 2D materials from degradation by oxygen and water.[11,31] Spencer *et al.* have used Al_2O_3 to encapsulate InSe-based FETs to prevent the exposure of InSe to air and demonstrated reproducible device operation even after six months of ambient exposure.[11] However, this encapsulation approach was adopted only after the device fabrication, resulting in the direct exposure of the InSe layer to the electron-beam resist and chemicals, which may account for the low electron mobility in the InSe channel (up to ~ 30 cm^2/Vs at room temperature). Here, we use an Al_2O_3 layer to encapsulate the surface of InSe immediately after its exfoliation, thus preventing the degradation of InSe before and after device fabrication. A self-aligned process and optimized excess etching are carried out on Al_2O_3-encapsulated InSe to define the source and drain contacts of the FET, which demonstrates a stable electrical performance over 50 days in air with a > 100% higher electron mobility (up to 857 cm^2/Vs at 300 K) and a factor of 10 smaller hysteresis than FETs fabricated using shadow masks. Furthermore, the FET exhibits a high, fast, and broad-band photoresponsivity. These findings

reveal figures of merits for InSe-phototransistors that exceed those reported to date in the present literature. The proposed fabrication could be extended to other 2D materials, including large-area wafer for scalability and high-precision pattern definition.

2. Result and Discussion

The schematic diagram in **Figure 1**a depicts our self-aligned fabrication process of InSe-based FETs. InSe flakes are exfoliated from bulk Bridgman-grown rhombohedral γ-InSe by adhesive tape and transferred onto a SiO_2/p-Si substrate. The unit cell of γ-InSe contains three layers, each consisting of four closely-packed and covalently bonded atomic sheets in the sequence Se-In-In-Se. A 30-nm-thick Al_2O_3 layer is grown on the as-prepared sample using ALD. Before depositing source and drain electrodes, the Al_2O_3 layer is etched using photolithography and inductively-coupled-plasma reactive-ion-etching system (ICP-RIE). A 10-nm-thick Ti layer and a 40-nm-thick Au layer are deposited using electron beam evaporation using the same photoresist mask for the ICP-RIE etching. Figure 1b shows the optical image of a typical InSe-based FET. The thickness of the InSe flake *t* is 4.0 nm, approximately five atomic layers, as measured using atomic-force microscopy (AFM) (Figure 1c).

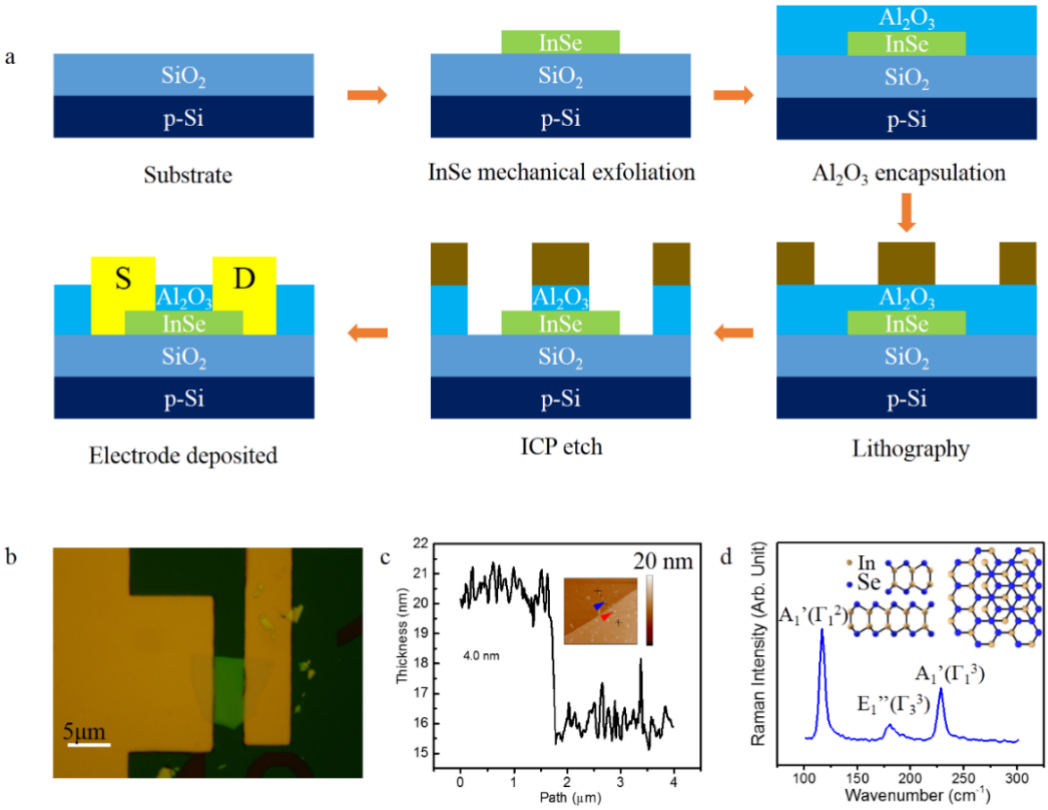

Figure 1. a) Schematic diagram illustrating the self-aligned fabrication process of InSe-based FETs. b) Optical image of an InSe FET. c) Thickness profile of the multilayer InSe obtained using AFM (inset: AFM image). d) Raman spectrum of a multilayer InSe flake measured using a 532 nm laser at 300 K (inset: crystal structure of InSe).

As shown in Figure 1d, the Raman spectrum of a multilayer InSe flake consists of three main peaks at 115, 178, and 228 cm^{-1}, corresponding to the vibrational modes $A_1'(\Gamma_1^2)$, $E''(\Gamma_3^3)$, and $A_1'(\Gamma_1^3)$, respectively, as reported before for high-quality InSe.[10] The Raman spectra of a 10-nm-thick InSe flake with the Al_2O_3 layer deposited immediately after the InSe exfoliation and without Al_2O_3 were studied over a period of 50 days, as shown in Figure S1 (Supporting Information). The Raman spectrum of the encapsulated InSe flake remains stable even after 50 days. In contrast, for the flake without the Al_2O_3 encapsulation, the intensity of the Raman peaks tends to degrade after just 10 days. This indicates that the prompt Al_2O_3 encapsulation of InSe after exfoliation can prevent the interaction of the InSe surface with oxygen and/or water in air.

The output and transfer characteristics of a 4-nm-thick InSe FET were measured using a probe station and an Agilent 2902A semiconductor analyzer at room temperature in the dark. The field effect electron mobility of the InSe FET can be extracted from the transfer characteristics, as shown in **Figure 2**a, using[32]

$$\mu = \frac{L}{W}\frac{1}{C_{\mathrm{i}}V_{\mathrm{ds}}}\frac{\mathrm{d}I_{\mathrm{ds}}}{\mathrm{d}V_{\mathrm{ds}}} \quad , \tag{1}$$

where C_{i} is the capacitance per unit area of the dielectric layer, W and L are the width and length of the InSe channel, I_{ds} is the drain current, and V_{ds} is the voltage between drain and source. The mobility of the encapsulated InSe FET is found to be $\mu = 857$ cm^2/Vs. FETs with different thicknesses t of InSe were fabricated to compare the encapsulation method described above with the standard shadow mask approach. The results in Figure 2b show that our self-aligned encapsulation method significantly improves the carrier mobility. Also, using the shadow mask method, we were not able to fabricate FETs with thin InSe (less than 20 nm) because of their small in-plane sizes (typical less than 20 μm). Benefiting from the Al_2O_3 encapsulation, the lithography-defined FET also exhibits a very small hysteresis, as shown in Figure 2a. The improvement of electrical performance is attributed to the Al_2O_3 encapsulation layer, which screens the chemical reactants in air, and to the photolithography process. In this work, the InSe flakes are passivated using Al_2O_3 immediately after the exfoliation, which is essential to achieve a much higher mobility compared with that of unpassivated InSe.[19,20] Separate experiments were performed to compare the characteristics of a bare FET before and after a delayed Al_2O_3 encapsulation (i.e., encapsulation after forming ohmic contacts on the InSe flake), as shown in Figure S2 (Supporting Information). The mobility and the contact resistance of the device remained almost the same before and after the Al_2O_3 encapsulation. This confirms that the

Al_2O_3 encapsulation soon after the exfoliation is essential to prevent the degradation of the InSe surface due to oxidation and adsorption of oxygen and water molecules in air.

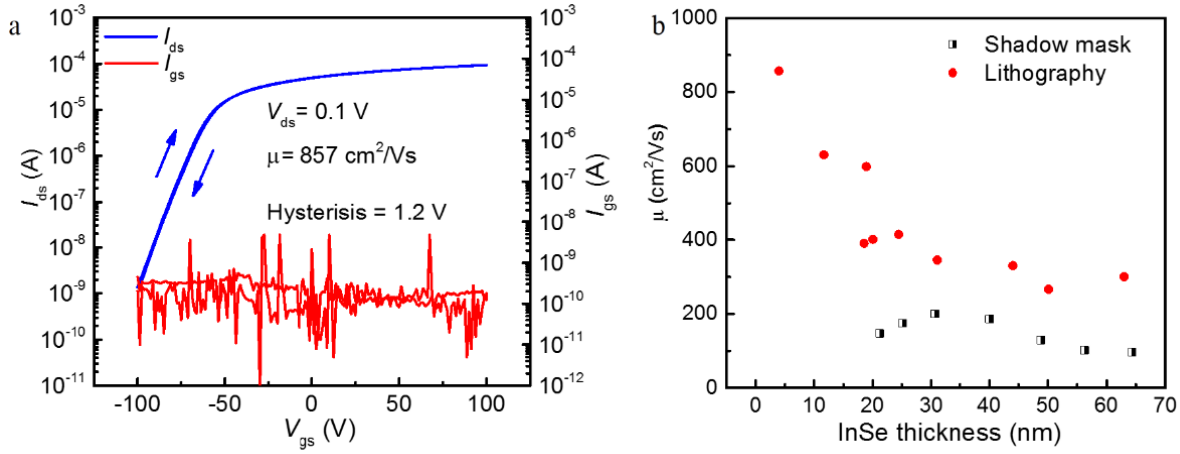

Figure 2. a) Transfer characteristics of a 4-nm-thick InSe FET at a drain voltage V_{ds} = 0.1 V under ambient conditions. b) Dependence of the field effect mobility of InSe FETs on the InSe layer thickness for devices fabricated via the shadow mask method and self-aligned encapsulation lithography.

Previous studies have shown that the electron mobility depends on the thickness of the InSe layer, revealing either an increase or decrease of μ with increasing layer thickness t.[19, 20, 33] As shown in Figure 2b, for our FETs with Al_2O_3-encapsulated InSe, the electron mobility tends to decrease with increasing t. This dependence is similar to that reported in Reference 20, where it was explained in terms of a simple resistor network model with interlayer resistors. Since the top layers are less directly impacted by the gate field screening effect, the mobility tends to degrade for thicker InSe layers. As shown in Figure S3 (Supporting Information), the interlayer resistance gradually dominates the source to drain resistance with increasing t.

Because of the irregular shape of InSe flakes, it is not appropriate to calculate the contact resistance (R_C) by the conventional transfer length method. Thus, we use the Y-function method to extract R_C from the transfer characteristics, as often done for 2D-material-based devices.[34]

We find that that for the Al_2O_3-passivated InSe FET, R_C = 0.18 kΩ, which is almost 50 times lower than the value of the FET fabricated using the shadow mask (R_C = 9.7 kΩ). More details can be found in Figure S4 (Supporting Information). The reason for such low contact resistance is twofold. Firstly, as the source and drain contacts are deposited immediately after the dry etching of Al_2O_3, the interface between InSe and the contacts is kept away from organic residues (PMMA or photoresist), oxygen and water. Secondly, excess etching tends to remove some of the InSe atomic layers in the contact areas. As a result, the contact resistance is significantly reduced due to a decrease in the interlayer resistance. The exact amount of excess etching is critical to achieve a low contact resistance R_C. Figure S5-6-7 (Supporting Information) shows the transfer characteristics of devices etched under different durations, showing a systematic dependence of R_C on the etching conditions: As the etching time increases beyond 170 s, the source-drain current, contact resistance and carrier mobility increase. However, if the etching time is too long, the source-drain current and the carrier mobility decrease, indicating an over etch of the InSe flake (the estimated etching rate for InSe is about 27 nm/min). An etching time of about 180 s is optimal for the excess etching and hence used for all the Al_2O_3 encapsulated devices. About 50 InSe devices were fabricated in about 10 rounds and all devices demonstrated consistent, reproducible results.

The Al_2O_3 encapsulation is beneficial to the stability and lifetime of the FETs, which are both critical for practical applications. The InSe FETs fabricated by shadow mask and self-aligned encapsulation lithography were exposed to air for 50 days. The corresponding transfer characteristics are plotted in **Figure 3**a and 3b. The field effect mobility of InSe FET without Al_2O_3 encapsulation decreases by about 53% from 170 to 80 cm^2/Vs after 50 days. Also, the

width of the hysteretic behavior in the transfer characteristics increases from 12 to 23 V. In contrast, for the Al_2O_3-encapsulated InSe FET, the field effect mobility decreases only by about 13% from 710 to 615 cm^2/Vs after 50 days. Also, the hysteresis remains very weak. The reason for such a significant improvement is twofold. Firstly, the contact resistance of the FET fabricated by self-aligned encapsulation lithography is much lower than that by the shadow mask. With the optimum excess etching, the contact resistance was reduced dramatically from 9.7 to 0.18 kΩ, which significantly enhances the carrier injection efficiency from the contact. Secondly, the Al_2O_3 encapsulation protects the InSe channel from oxygen and water, resulting in much reduced surface states and improved effective mobility than when storing in ambient air. The slight reduction in mobility may arise from a partial degradation of Al_2O_3. For example, the oxygen transmission rate through a 30 nm-thick Al_2O_3 was found to be 1.96 $cc/m^2/day$.[35] For a 26 nm Al_2O_3 layer, the water transmission rate is about 1×10^{-3} $g/m^2/day$.[36] Compared to conventional thin films, 2D materials are more sensitive to the external environment.[13,14] From Figure 3c, it is clear that the carrier mobility for the Al_2O_3-encapsulated InSe improves significantly by 514% as compared to that of the unencapsulated InSe. Such an improvement becomes even more pronounced (767%) after 50 days of exposure of the device to air. Similarly, the hysteresis is reduced by a factor of 7 just after the fabrication and by a factor of 13 after 50 days of exposure to air. The threshold voltages of the device in Figure S2 before and after the "delayed" encapsulation were 2.6 and 1.4 V, respectively. In contrast, when InSe flake was immediately encapsulated by Al_2O_3 after exfoliation, the threshold voltage showed a large reduction even after 50 days of storage, as shown in Figures 3a and 3b, demonstrating an effective prevention of degradation. The different behavior of the two devices is shown in

Figure 3c and 3d, demonstrating the effectiveness of the prompt Al_2O_3 encapsulation and the self-aligned process. It should be pointed that the deposition of Al_2O_3 may introduce some damage to the surface of the InSe flakes. Nevertheless, the experiments showed that any damage by deposition should be less severe than the rapid degradation of the InSe surface properties, as illustrated by the strong contrast between the device performance in Figure 3a (without encapsulation) and Figure 3b (with encapsulation). Therefore, the benefit significantly outweighs any potential damage. The prompt encapsulation method and self-aligned electrical contacts developed in this work may be used to improve and stabilize the performance of other 2D materials.

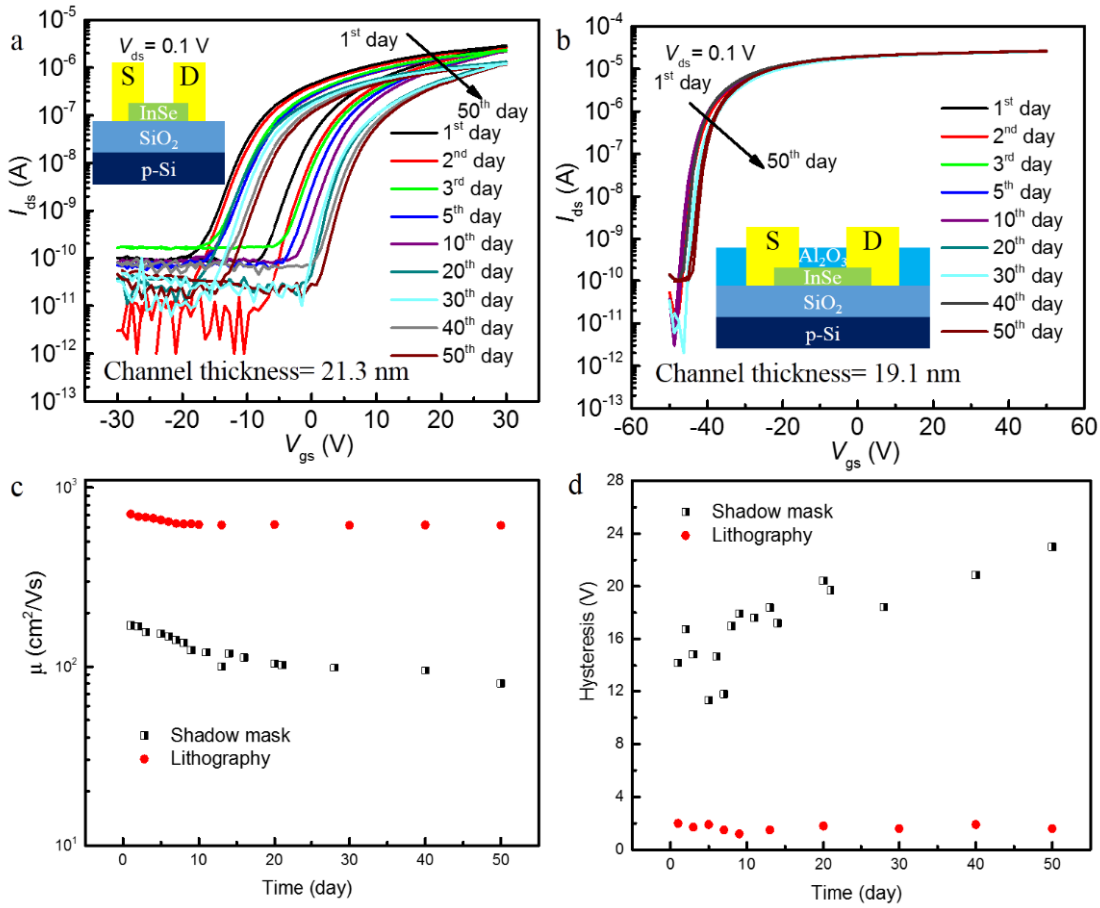

Figure 3. Time evolution of the transfer characteristics of InSe FETs fabricated by a) shadow mask and b) self-aligned encapsulation lithography under ambient conditions. Time evolution

of c) field effect mobility and d) hysteresis of InSe FETs made by shadow mask and self-aligned encapsulation lithography under ambient conditions.

We now examine the photoresponse of the InSe FETs. In order to test the photoresponse, monochromatic light (λ = 450 nm) was used to illuminate the InSe channel in ambient conditions. One determinant figure of merit of the photodetector is the responsivity ($R = I_{ph}/SP_{inc}$),[37] which is defined as the ratio of the photocurrent I_{ph} to SP_{inc}. Here, P_{inc} is the laser power density incident on the device and S is the area of the InSe channel. As shown in Figure S8 (Supporting Information), the responsivity of the Al_2O_3-encapsulated InSe FET using SiO_2 as the dielectric layer is $R = 2.3 \times 10^7$ A/W at V_{gs} = 40 V for P_{inc} = 1 μW/cm^2, which is comparable to the values of R for FET-photodetectors previously obtained in vacuum.[11] By using Al_2O_3 as the gate dielectric layer, the responsivity of the InSe FET is further improved. **Figure 4**a shows the transfer characteristics of InSe FET phototransistors with Al_2O_3 used as the gate dielectric layer at various illumination intensities and V_{ds} = 1 V. By changing the gate dielectric material from SiO_2 to Al_2O_3 and reducing the dielectric thickness, the InSe FET can be switched off at a low voltage (around 0 V) with an on/off ratio above 10^7 (before illumination). Figure 4b shows the responsivity as a function of P_{inc}. The linear dependence of the responsivity on P_{inc} in the log scale indicates a power dependence described by the empirical equation[21,38]

$$R = \frac{I_{ph}}{SP_{inc}} = \frac{\alpha P_{inc}^{\beta}}{SP_{inc}} = \frac{\alpha P_{inc}^{\beta-1}}{S}, \quad (2)$$

where β is a constant. A fit to the data gives β = 0.28 for P_{inc} in the range from 0.001 to 20 mW/cm^2, which is comparable to the value of 0.30 obtained by Luo *et al.*[21] Different mechanisms can contribute to the sublinear dependence of R on P_{inc}: [7,21,38] The transit time τ_e

of majority carriers (electrons) in the InSe channel tends to increase with P_{inc} due to enhanced carrier scattering, thus decreasing R; furthermore, the lifetime of minority holes τ_h is limited by defects and charged impurities and is reduced at high carrier densities (or high P_{inc}) due to Auger recombination. In turn, this reduces the internal gain and responsivity that scale as τ_h/τ_e.[7] The highest responsivity ($R = 2.1\times10^8$ A/W) is obtained at $V_{ds} = 1$ V and $V_{gs} = 9.5$ V, which is almost 10 times higher than the value obtained using SiO_2 as the gate dielectrics.

Another key parameter of the detection performance is the specific detectivity (D^*)

$$D^* = \frac{RS^{\frac{1}{2}}}{S_n}, \tag{3}$$

where S_n is the current noise spectral density.[39] From the measured noise spectrum (see Figure S9 in Supporting Information) and Equation 3, we find that $D^* = 1.9\times10^{13}$ Jones for $R = 2.1\times10^8$ A/W. Table 1 compares our values of R and D^* with those from the literature. To the best of our knowledge, these values are amongst the highest and R is about one order of magnitude larger than the best values reported in the literature.

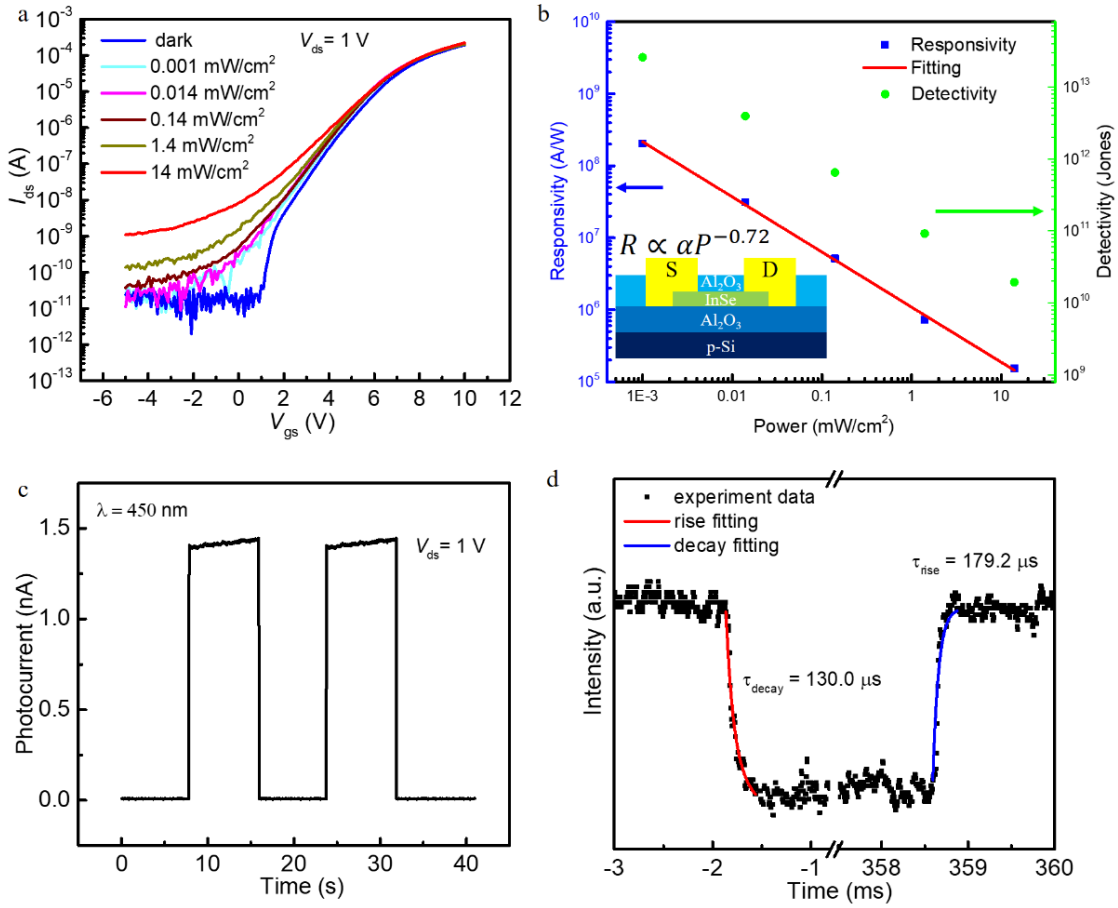

Figure 4. a) Typical transfer characteristics of InSe FETs with illumination at various intensities (0.001, 0.014, 0.14, 1.4, 14 mW/cm^2) at V_{ds} = 1 V. b) Responsivity (blue squares) and detectivity (green dots) as a function of illumination intensity at V_{ds} = 1 V and V_{gs} = 9.5 V. c) Time-resolved photocurrent response of the InSe photodetector. d) Rise and decay times of the device extracted from the temporal dependence of the photocurrent.

Table 1. Summary of 2D-material-based photodetectors in literature

Materials	Spectral range (nm)	R (A/W)	D* (Jones)	τ (ms)	Reference
InSe	516	2.0×10^7	*	*	[11]
InSe	543	*	*	0.087	[40]
InSe	325	1.8×10^7	1.1×10^{15}	7000	[41]
InSe	700	1.7×10^4	9.1×10^{12}	20	[42]
InSe	405	1.0×10^5	7.3×10^{12}	0.5/26	[39]
WSe_2	650	1.8×10^5	10^{14}	23	[43]
WSe_2	735	0.6	10^{13}	0.008	[18]
MoS_2	561	880	1.7×10^{14}	9000	[44]
BP	400-3750	0.0072	*	0.04/0.04	[45]
BP	633	4.3×10^6	*	5	[46]
In_2Se_3	300	395	2.3×10^{12}	18	[47]
InSe	**450**	**2.1×10^8**	**1.9×10^{13}**	**0.179/0.130**	**This work**

Photodetection experiments were conducted on devices with different thickness of the InSe layer and $\lambda = 450$ nm, as shown in Figure S10 (Supporting Information). The responsivity of InSe photodetector first increases once the InSe thickness increases, then decreases as the thickness is larger than 25 nm. Feng *et al.* calculated the total photo absorption in InSe layers with different thicknesses and also found a maximum peak absorption around 30 nm.[46] We further studied the responsivity at different illumination wavelengths. As shown in Figure S11 (Supporting Information), the responsivity of InSe photodetector tends to increase as the wavelength of illumination light decreases, which can be explained by the increased absorption at shorter wavelengths.[49]

The response times, including rise and decay times, are key performance parameters for a detector and can be obtained using simple exponential dependences of the current versus time.[50] The response time depends on defects, charged impurities, and trap states induced by adsorbed molecules.[39,41,42] The response time in Table 1 ranges from several microseconds to several seconds.[39-42] Figure 4c shows the transient photocurrent of the InSe photodetector

measured under a bias of 1 V. As shown in Figure 4d, the rise and decay times are ~ 179 and 130 μs, respectively, which compare favorably with the temporal response of 2D-material-based photodetectors. Such fast response times indicate a high quality 2D layer and effective screening of polar or charged impurities using the prompt Al_2O_3 encapsulation.

3. Conclusion

InSe transistors and photodetectors have been fabricated by combining self-aligned photolithography, a prompt Al_2O_3 encapsulation, and an appropriate excess etching, leading to substantial improvements in carrier transport and photoresponse. The InSe photodetectors exhibit a responsivity of up to 2.1×10^8 A/W, which is at least one order of magnitude better than in previous devices based on InSe and other 2D materials. The devices also remain stable over 50 days of exposure in air. This work provides an effective method to improve the lithography process tolerance, air stability, and optoelectronic performance of InSe. The proposed method of fabrication could be applied to other 2D materials, providing a route to scalable and reproducible fabrication of devices for science and technologies.

4. Methods

4.1 Device Fabrication

Si/SiO_2 and Si (P^{++}) substrates were cleaned using deionized water, acetone, and ethanol. The substrate was then etched using buffered oxide etch (BOE) solution (1% in volume ratio) for 1 minute at room temperature. The Al_2O_3 film was deposited using ALD at 0.15 mTorr and 150 ºC with a growth rate of 0.1 nm/cycle. A direct laser writer (MicroWriter ML®2) was used to pattern the devices. The Al_2O_3 layer was etched by an inductive coupled plasma etch (PlasmaPro® 100 Cobra, Oxford Instrements) with ICP power, HF power, chamber pressure,

gas flow, and etching time of 50 W, 100 W, 8 mTorr, BCl_3 (15 sccm) and 3 minutes, respectively. For Al_2O_3 gated devices, Si (P^{++}) was used as a gate and 30-nm-thick Al_2O_3 film was deposited using ALD at 0.15 mTorr and 150 ºC with a growth rate of 0.1 nm/cycle.

The InSe flakes were obtained by mechanical exfoliation developed by Novoslev *et al*. A piece of Nitto tape (BT-150-KL) was first pressed onto a bulk InSe crystal and then peeled off slowly. The tape was then pressed onto another tape and peeled off again. The process was repeated a few times until InSe nanosheets with appropriate thickness were achieved. Finally, the tape was pressed onto the substrate to complete the InSe nanosheets transfer.

4.2 Photoresponse Measurements

The intensity of the incident laser source (λ = 450 nm) was measured using a power and energy meter (SUSS UV-optometer). The response times of the as fabricated InSe photodetector were measured using a 450 nm laser source at a chopping frequency of 1 Hz. The photocurrent was measured using an oscilloscope (UTD2012CM) at 500 kHz.

Supporting Information

Supporting Information is available from the Wiley Online Library or from the author.

Acknowledgements

This work was financed by National Key Research and Development Program of China (No. 2016YFA0301200), National Natural Science Foundation of China (No. 11374185), Engineering and Physical Sciences Research Council (EPSRC) (No. EP/N021258/1), the Royal Society grants IEC\R2\170155 and NA170415, the Key Research and Development Program of Shandong Province (2017GGX10111), the Natural Science Foundation of Shandong Province (ZR2013FM033 and ZR2018MF029), the Fundamental Research Funds of Shandong University (2016WLJH44) and the European Union's Horizon 2020 research and innovation programmer under grant agreement Graphene Core3.

Conflict of Interest

The authors declare no conflict of interest.

References

[1] K. S. Novoselov, A. K. Geim, S. V. Morozov, D. Jiang, Y. Zhang, S. V. Dubonos, I. V. Grigorieva, A. A. Firsov, *Science* **2004**, 306, 666.

[2] K. S. Novoselov, A. K. Geim, S. V. Morozov, D. Jiang, M. I. Katsnelson, I. V. Grigorieva, S. V. Dubonos, A. A. Firsov, *Nature* **2005**, 438, 197.

[3] D. Krasnozhon, D. Lembke, C. Nyffeler, Y. Leblebici, A. Kis, *Nano Lett.* **2014**, 14, 5905.

[4] X. J. Xie, D. Sarkar, W. Liu, J. H. Kang, O. Marinov, M. J. Deen, K. Banerjee, *ACS Nano* **2014**, 8, 5633.

[5] L. Li, Y. Yu, G. J. Ye, Q. Ge, X. Ou, H. Wu, D. Feng, X. H. Chen, Y. Zhang, *Nature Nanotech.* **2014**, 9, 372.

[6] G. W. Mudd, S. A. Svatek, T. Ren, A. Patane, O. Makarovsky, L. Eaves, P. H. Beton, Z. D. Kovalyuk, G. V. Lashkarev, Z. R. Kudrynskyi, A. I. Dmitriev, *Adv. Mater.* **2013**, 25, 5714.

[7] G. W. Mudd, S. A. Svatek, L. Hague, O. Makarovsky, Z. R. Kudrynskyi, C. J. Mellor, P. H. Beton, L. Eaves, K. S. Novoselov, Z. D. Kovalyuk, E. E. Vdovin, A. J. Marsden, N. R. Wilson, A. Patane, *Adv. Mater.* **2015**, 27, 3760.

[8] D. A. Bandurin, A. V. Tyurnina, G. L. Yu, A. Mishchenko, V. Zólyomi, S. V. Morozov, R. K. Kumar, R. V. Gorbachev, Z. R. Kudrynskyi, S. Pezzini, Z. D. Kovalyuk, U. Zeitler, K. S. Novoselov, A. Patanè, L. Eaves, I. V. Grigorieva, V. I. Fal'ko, A. K. Geim, Y. Cao, *Nature Nanotech.* **2016**, 12, 223.

[9] F. G. Yan, C. Hu, Z. A. Wang, H. L. Lin, K. Y. Wang, *Appl. Phys. Lett.* **2021**, 118, 19.

[10] S. Lei, L. Ge, S. Najmaei, A. George, R. Kappera, J. Lou, M. Chhowalla, H. Yamaguchi, G. Gupta, R. Vajtai, A. D. Mohite, P. M. Ajayan, *ACS Nano* **2014**, 8, 1263.

[11] S. A. Wells, A. Henning, J. T. Gish, V. K. Sangwan, L. J. Lauhon, M. C. Hersam, *Nano Lett.* **2018**, 18, 7876.

[12] P. H. Ho, Y. R. Chang, Y. C. Chu, M. K. Li, C. A. Tsai, W. H. Wang, C. H. Ho, C. W. Chen, P. W. Chiu, *ACS Nano* **2017**, 11, 7362.

[13] X. Wei, C. Dong, A. Xu, X. Li, D. D. Macdonald, *Phys. Chem. Chem. Phys.* **2018**, 20, 2238.

[14] L. Shi, Q. Zhou, Y. Zhao, Y. Ouyang, C. Ling, Q. Li, J. Wang, *J. Phys. Chem. Lett.* **2017**, 8, 4368.

[15] T. Wang, K. Andrews, A. Bowman, T. Hong, M. Koehler, J. Yan, D. Mandrus, Z. Zhou, Y. Q. Xu, *Nano Lett.* **2018**, 18, 2766.

[16] Y. Jia, X. Gong, P. Peng, Z. Wang, Z. Tian, L. Ren, Y. Fu, H. Zhang, *Nano-micro Lett.* **2016**, 8, 336.

[17] K. Jin, T. Li, H. Cai, M. Li, N. Pan, X. Wang, *Opt. Commun.* **2019**, 436, 47.

[18] Y. T. Huang, Y. H. Chen, Y. J. Ho, S. W. Huang, Y. R. Chang, K. Watanabe, T. Taniguchi, H. C. Chiu, C. T. Liang, R. Sankar, F. C. Chou, C. W. Chen, W. H. Wang, *ACS Appl. Mater. Interfaces* **2018**, 10, 33450.

[19] W. Feng, W. Zheng, W. Cao, P. Hu, *Adv. Mater.* **2014**, 26, 6587.

[20] G. Liang, Y. Wang, L. Han, Z. X. Yang, Q. Xin, Z. R. Kudrynskyi, Z. D. Kovalyuk, A. Patanè, A. Song, *Semicond. Sci. Technol.* **2018**, 33, 06LT01.

[21] W. Luo, Y. Cao, P. Hu, K. Cai, Q. Feng, F. Yan, T. Yan, X. Zhang, K. Wang, *Adv. Opt. Mater.* **2015**, 3, 1418.

[22] Y. Wang, J. Zhang, G. Liang, Y. Shi, Y. Zhang, Z. R. Kudrynskyi, Z. D. Kovalyuk, A. Patanè, Q. Xin, A. Song, *Appl. Phys. Lett.* **2019**, 115, 033502.

[23] J. Jiang, J. Li, Y. Li, J. Duan, L. Li, Y. Tian, Z. Zong, H. Zheng, X. Feng, Q. Li, H. Liu, Y. Zhang, T. L. Ren, L. Han, *NPJ 2D Mater. Appl.* **2019**, 3, 29.

[24] J. D. Wood, S. A. Wells, D. Jariwala, K. S. Chen, E. Cho, V. K. Sangwan, X. Liu, L. J. Lauhon, T. J. Marks, M. C. Hersam, *Nano Lett.* **2014**, 14, 6964.

[25] A. Politano, G. Chiarello, R. Samnakay, G. Liu, B. Gurbulak, S. Duman, A. A. Balandin, D. W. Boukhvalov, *Nanoscale* **2016**, 8, 8474.

[26] Z. Li, H. Qiao, Z. Guo, X. Ren, Z. Huang, X. Qi, S. C. Dhanabalan, J. S. Ponraj, D. Zhang, J. Li, J. Zhao, J. Zhong, H. Zhang, *Adv. Funct. Mater.* **2018**, 28, 1705237.

[27] H. Arora, Y. Jung, T. Venanzi, K. Watanabe, T. Taniguchi, R. Hubner, H. Schneider, M. Helm, J. C. Hone, A. Erbe, *ACS Appl. Mater. Interfaces* **2019**, 11, 43480.
[28] J. Robertson, R. Wallace, *Mater. Sci. Eng. R Rep.* **2015**, 88, 1.
[29] P. Ma, L. Du, Y. Wang, R. Jiang, Q. Xin, Y. Li, A. Song, *Appl. Phys. Lett.* **2018**, 112, 023501.
[30] P. Ma, W. Guo, J. Sun, J. Gao, G. Zhang, Q. Xin, Y. Li, A. Song, *Semicond. Sci. Technol.* **2019**, 34, 105004.
[31] S. Hong, H. Im, Y. K. Hong, N. Liu, S. Kim, J. H. Park, *Adv. Electron Mater.* **2018**, 4, 1800308.
[32] S. Sucharitakul, N. J. Goble, U. R. Kumar, R. Sankar, Z. A. Bogorad, F. C. Chou, Y. T. Chen, X. P. Gao, *Nano Lett.* **2015**, 15, 3815.
[33] S. Das, H. Y. Chen, A. V. Penumatcha, J. Appenzeller, *Nano Lett.* **2013**, 13, 100.
[34] S. Bhattacharjee, K. L. Ganapathi, D. N. Nath, N. Bhat, *IEEE Electron Dev. Lett.* **2016**, 37, 119.
[35] W. Lei, X. Li, Q. Chen, Z. Wang, *Plasma Sci. Technol.* **2012**, 14, 129.
[36] M. D. Groner, S. M. George, R. S. McLean, P. F. Carcia, *Appl. Phys. Lett.* **2006**, 88, 051907.
[37] Y. Liu, L. Du, G. Liang, W. Mu, Z. Jia, M. Xu, Q. Xin, X. Tao, A. Song, *IEEE Electron Dev. Lett.* **2018**, 39, 1696.
[38] S. R. Tamalampudi, Y. Y. Lu, R. Kumar U, R. Sankar, C. D. Liao, K. Moorthy B, C. H. Cheng, F. C. Chou, Y. T. Chen, *Nano Lett.* **2014**, 14, 2800.
[39] Y. Yang, J. Jeon, J. H. Park, M. S. Jeong, B. H. Lee, E. Hwang, S. Lee, *ACS Nano* **2019**, 13, 8804.
[40] S. Lei, F. Wen, L. Ge, S. Najmaei, A. George, Y. Gong, W. Gao, Z. Jin, B. Li, J. Lou, J. Kono, R. Vajtai, P. Ajayan, N. J. Halas, *Nano Lett.* **2015**, 15, 3048.
[41] H. W. Yang, H. F. Hsieh, R. S. Chen, C. H. Ho, K. Y. Lee, L. C. Chao, *ACS Appl. Mater. Interfaces* **2018**, 10, 5740.
[42] W. Feng, F. Qin, M. Yu, F. Gao, M. Dai, Y. Hu, L. Wang, J. Hou, B. Li, P. Hu, *ACS Appl. Mater. Interfaces* **2019**.
[43] W. Liu, J. Kang, D. Sarkar, Y. Khatami, D. Jena, K. Banerjee, *Nano Lett.* **2013**, 13, 1983.
[44] O. Lopez-Sanchez, D. Lembke, M. Kayci, A. Radenovic, A. Kis, *Nature Nanotech.* **2013**, 8, 497.
[45] H. Yuan, X. Liu, F. Afshinmanesh, W. Li, G. Xu, J. Sun, B. Lian, A. G. Curto, G. Ye, Y. Hikita, Z. Shen, S. C. Zhang, X. Chen, M. Brongersma, H. Y. Hwang, Y. Cui, *Nature Nanotech.* **2015**, 10, 707.
[46] M. Huang, M. Wang, C. Chen, Z. Ma, X. Li, J. Han, Y. Wu, *Adv. Mater.* **2016**, 28, 3481.
[47] R. B. Jacobs-Gedrim, M. Shanmugam, N. Jain, C. A. Durcan, M. T. Murphy, T. M. Murray, R. J. Matyi, R. L. Moore, II, B. Yu, *ACS Nano* **2014**, 8, 514.
[48] W. Feng, J. B. Wu, X. Li, W. Zheng, X. Zhou, K. Xiao, W. Cao, B. Yang, J. C. Idrobo, L. Basile, W. Tian, P. Tan, P. Hu, *J. Mater. Chem. C* **2015**, 3, 7022.
[49] M. Dai, H. Chen, R. Feng, W. Feng, Y. Hu, H. Yang, G. Liu, X. Chen, J. Zhang, C. Y. Xu, P. Hu, *ACS Nano* **2018**, 12, 8739.
[50] S. Cui, Z. Mei, Y. Zhang, H. Liang, X. Du, *Adv. Opt. Mater.* **2017**, 5, 1700454.

Supporting Information

Significant Performance Enhancement of InSe-Phototransistors by Al_2O_3 Encapsulation

Guangda Liang, Yiming Wang, Jiawei Zhang, Zakhar R. Kudrynskyi, Zakhar Kovalyuk, Amalia Patanè, Qian Xin*, and Aimin Song**

S1. Raman Spectroscopy

The Raman spectrum of the InSe flake with the Al_2O_3 encapsulation does not change significantly after 50 days. In contrast, the flake without the Al_2O_3 encapsulation degrades significantly with time, as shown in Figure S1. The experiments indicate that the Al_2O_3 encapsulation can prevent the degradation of InSe in air.

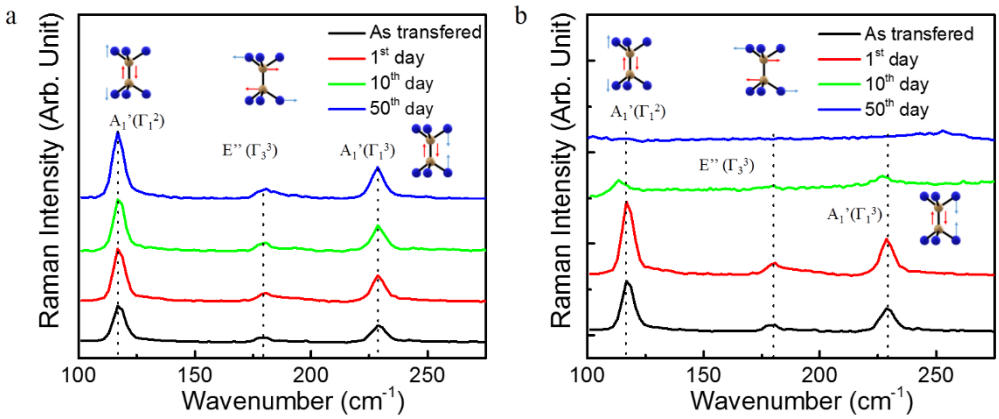

Figure S1. Time evolution of the Raman spectra of InSe flakes a) with and b) without Al_2O_3 encapsulation from the time in which the InSe flakes are transferred to 50 days after the transfer.

S2. Transfer Characteristics

The characteristics of the bare FET before and after a delayed Al_2O_3 encapsulation are shown in Figure S2. The mobility and the contact resistance of the device remain almost the same before and after the Al_2O_3 encapsulation.

The metal source and drain contacts are connected only directly to the top InSe layer (R_n is the resistance of nth layer InSe), while access to the bottom layers involves an additional interlayer resistance (R_{int}). The interlayer resistance tends to gradually dominate the total resistance with increasing the InSe layer thickness. Thus, the effective field mobility decreases as the InSe thickness increases.[1]

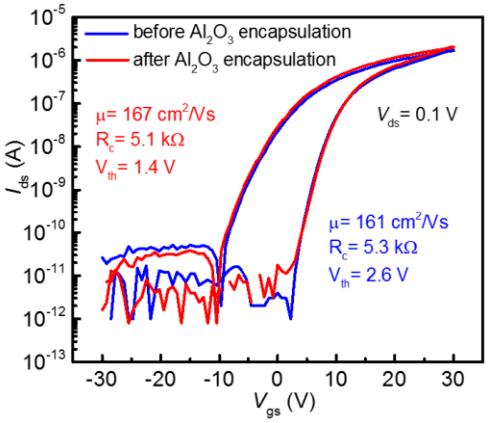

Figure S2. Transfer characteristics of the bare FET before and after a delayed Al_2O_3 encapsulation.

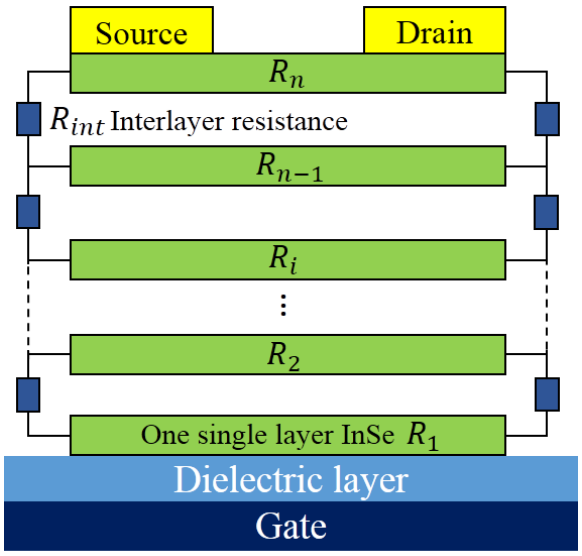

Figure S3. Interlayer resistor network model.

S3. Y-Model and Contact Resistance

The drain current of the FET can be expressed as

$$I_{\mathrm{ds}} = \frac{WC_{\mathrm{ox}}}{L}\frac{\mu_0}{\left[1+\theta\left(V_{\mathrm{gs}}-V_{\mathrm{th}}\right)\right]}\left(V_{\mathrm{gs}}-V_{\mathrm{th}}\right)V_{\mathrm{ds}} \ , \tag{S1}$$

where V_{th} is the threshold voltage, θ is the intrinsic mobility degradation factor due to remote phonon scattering and surface roughness, and can be expressed as[2,3]

$$\theta = \theta_0 + R_{\mathrm{c}}C_{\mathrm{ox}}\mu_0\frac{W}{L} \ . \tag{S2}$$

In the limit of a negligible θ_0, θ can be approximated as

$$\theta \approx R_{\mathrm{c}}C_{\mathrm{ox}}\mu_0\frac{W}{L} \ . \tag{S3}$$

The transconductance $g_{\mathrm{m}} = dI_{\mathrm{ds}}/dV_{\mathrm{gs}}$ can be expressed as

$$g_{\mathrm{m}} = \frac{WC_{\mathrm{ox}}}{L}\frac{\mu_0}{\left[1+\theta\left(V_{\mathrm{gs}}-V_{\mathrm{th}}\right)\right]^2}V_{\mathrm{ds}} \ . \tag{S4}$$

We define the Y as

$$\mathrm{Y} = \frac{I_{\mathrm{ds}}}{g_{\mathrm{m}}^{1/2}} = \left(\frac{W}{L}C_{\mathrm{ox}}\mu_0 V_{\mathrm{ds}}\right)^{1/2}\left(V_{\mathrm{gs}}-V_{\mathrm{th}}\right) \tag{S5}$$

and

$$g_{\mathrm{m}}^{-1/2} = \frac{WC_{\mathrm{ox}}\mu_0 V_{\mathrm{ds}}}{L}^{-1/2}\left[1+\theta\left(V_{\mathrm{gs}}-V_{\mathrm{th}}\right)\right]. \tag{S6}$$

From the slope of the linear fitting of the dependence of the Y parameter on V_{gs}, we can extract the field effect mobility μ_0.[4] From the slope of the linear fitting of the dependence of $g_{\mathrm{m}}^{-1/2}$ on V_{gs}, we can extract θ and R_{c}.[5,6] The Y-method has been used in previous studies of 2D materials, such as MoS_2,[7-11] $MoSe_2$,[12] ReS_2,[13] BP,[14,15] InSe,[16,17] and other semiconductors[18-21]. For example, by comparing the Y-function method and the corrected TLM method, Chang *et al.* verified that the Y-function method can be adopted as a convenient way to estimate R_{c}.[9]

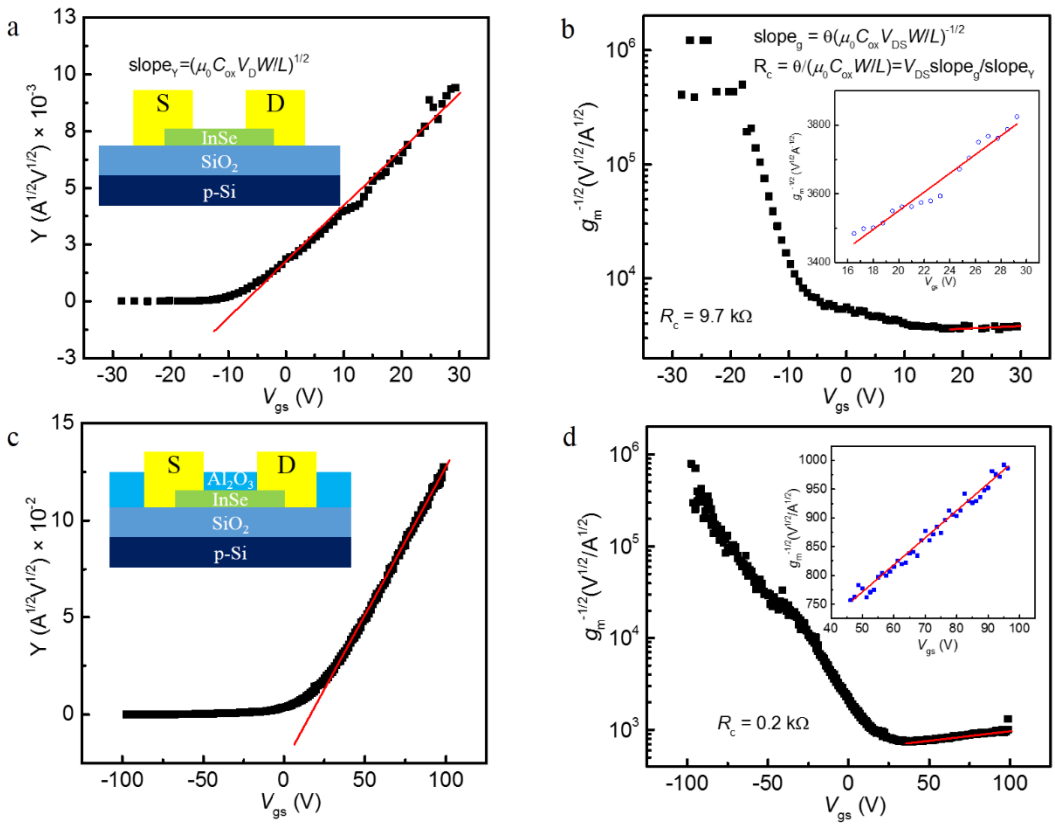

Figure S4. a) Y and b) $g_{\mathrm{m}}^{-1/2}$ as a function of V_{gs} for an InSe FET fabricated by shadow mask. c) Y and d) $g_{\mathrm{m}}^{-1/2}$ as a function of V_{gs} for an Al_2O_3 encapsulated InSe FET fabricated by lithography.

The contact resistance of the Al_2O_3 encapsulated InSe FET fabricated by lithography is R_c = 0.18 kΩ, which is 48 times lower than that for the FET fabricated by shadow mask (R_c = 9.7 kΩ). This contact resistance is, to the best of our knowledge, at least one order of magnitude lower than the best data in the literature, as shown in Table S1.

Table S1 Contact resistances in the literature

R_c (kΩ)	Fabrication method	Reference
506/2.4	Shadow mask	[22]
44.0	Electron beam lithography	[16]
3.8	Shadow mask	[23]
15.0	Shadow mask	[24]
9.7	Shadow mask	This work
0.18	Al_2O_3 encapsulation lithography	This work

S4. Etching

We have observed an etching rate of 11.5 nm/min for Al_2O_3, as shown in Figure S5a. BCl_3 can also etch the InSe layer after etching Al_2O_3. If the etching time is too long, the region of the InSe layer under the source/drain contacts can be almost totally etched, as shown in Figure S5b for an etching time of 190 s. Such excess etching results in a large contact resistance and a low effective mobility. On the other hand, if the etching time is too short, the residual Al_2O_3 prevents the conduction between the InSe layer and the contacts, also resulting in a low effective mobility, as shown in Figure S5b for an etching time of 170 s.

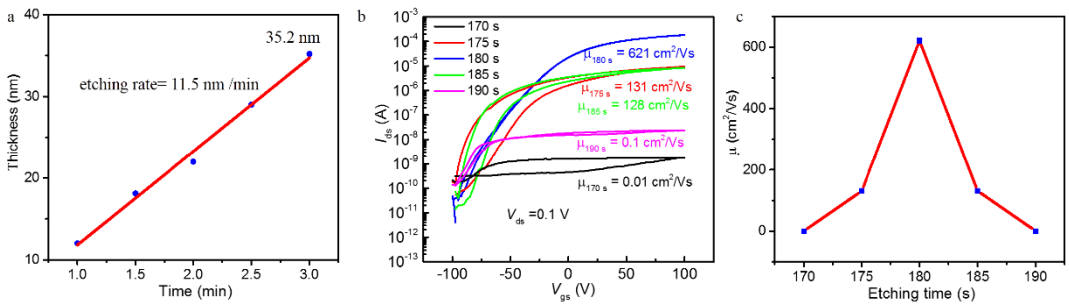

Figure S5. a) Etching thickness versus etching time. b) Transfer characteristics of devices with different etching times (170, 175, 180, 185 and 190 s). The thickness of the channels is around 15 nm. c) Electron mobility versus etching time.

Figure S6 shows the AFM image of an InSe flake capped with Al_2O_3. The surface roughness of the Al_2O_3/InSe structure is 1.17 nm.

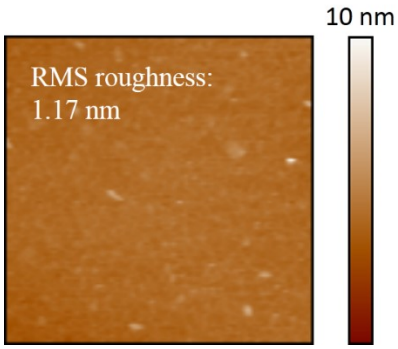

Figure S6. AFM image of an InSe flake capped with Al_2O_3.

The SEM images in Figures S7a, b and c show the cross-sections of the Al_2O_3 layer with etching times of a) 1 min, b) 2 min and c) 3 min. The AFM images in Figures S7d, e and f show etching thicknesses of 12.0, 22.3 and 35.2 nm, respectively.

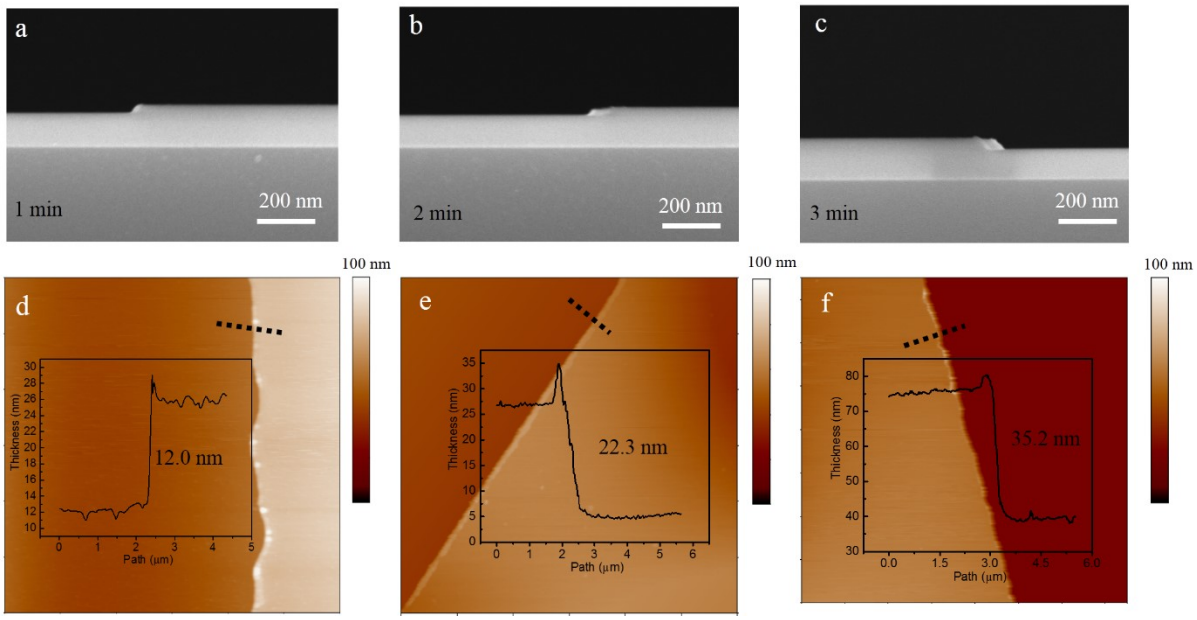

Figure S7. SEM images of cross-section of Al_2O_3 with etching times of a) 1 min, b) 2 min and c) 3 min. AFM images showing etching thicknesses of 12.0, 22.3 and 35.2 nm, respectively.

S5. Photoresponse

The detectivity (D^*) of a photodetector is determined by the current noise, S_n, and the photoresponsivity, R. To estimate D^*, we have measured the transfer characteristics (Figure S8)

and the drain current noise spectral density (Figure S9) of InSe FETs with an InSe layer thickness of 15 nm. The noise spectral density was measured using an optical chopper for modulation of light. We estimate S_n, the noise equivalent powers (*NEP*) and *D** at f=100 Hz. For the Al_2O_3 gated encapsulated InSe device, S_n = 2.3 × 10^{-11} A/Hz$^{0.5}$, D^* = 1.9 × 10^{13} Jones, and *NEP* = 3.6 × 10^{-19} W/Hz$^{0.5}$ at f=100 Hz, λ = 450 nm, incident power of 1 μW/cm^2, V_{ds} = 1 V and V_{gs} = 9.5 V. For the SiO_2 gated encapsulation InSe device, S_n = 3.4 × 10^{-11} A/Hz$^{0.5}$, D^* = 7.5 × 10^{12} Jones, and *NEP* = 1.5 × 10^{-18} W/Hz$^{0.5}$, at f=100 Hz, λ = 450 nm, incident power of 1 μW/cm^2, V_{ds} = 1 V and V_{gs} = 40 V.

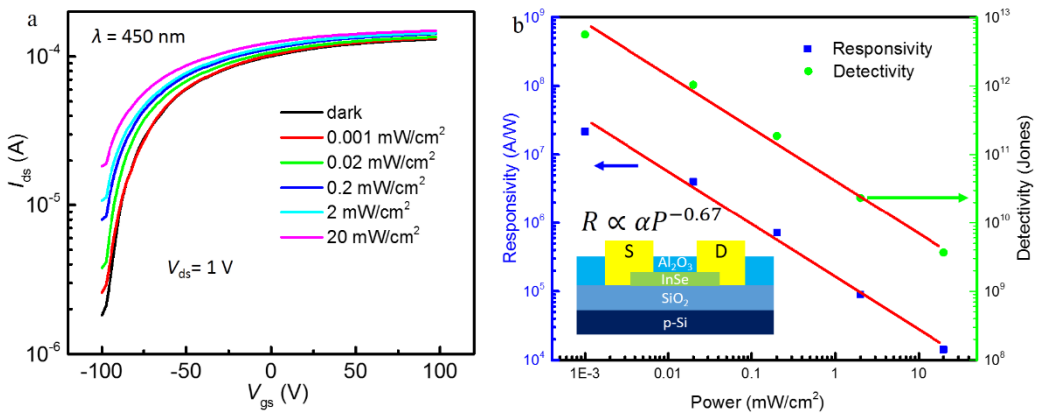

Figure S8. a) Typical transfer characteristics of InSe FETs with SiO_2 as gate dielectric at various illumination intensities (0.001, 0.02, 0.2, 2, 20 mW/cm^2) at V_{ds} = 1 V and λ = 450. b) Responsivity (blue squares) and detectivity (green dots) as a function of illumination intensity at V_{ds} = 1 V and V_{gs} = 40 V.

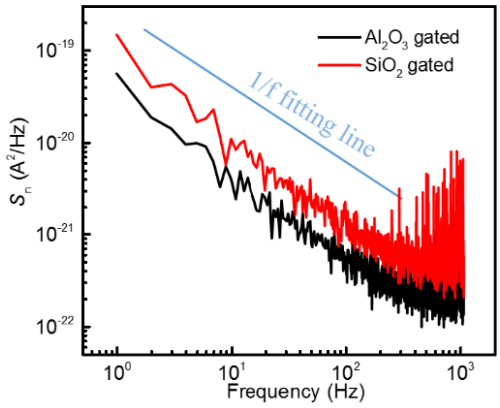

Figure S9. Low frequency noise (S_n) versus frequency for Al_2O_3 and SiO_2 gated InSe photodetectors.

We have examined the photoresponsivity of FETs with different InSe layer thickness. For a given laser wavelength λ = 450 nm, with increasing layer thickness the value of R first increases, as shown in Figure S10. The photoresponsivity then decreases as the thickness becomes larger than 25 nm. Feng *et al.* calculated the total photo absorption in InSe layers with different thicknesses, and found a maximum absorption around 30 nm at λ = 450 nm.[25]

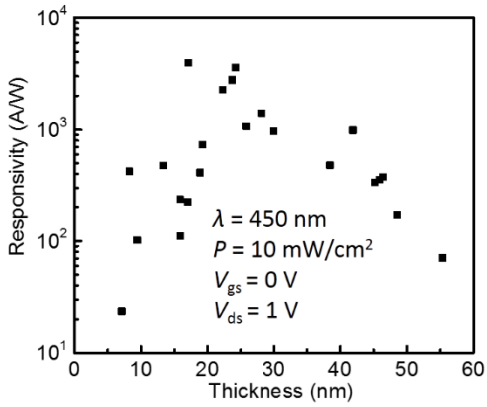

Figure S10. Responsivity as a function of the InSe layer thickness under illumination with laser light of intensity of 10 mW/cm^2 and λ = 450 nm at V_{ds} = 1 V and V_{gs} = 0 V.

Figure S11 shows that the responsivity of an InSe photodetector (InSe layer thickness of 12 nm) increases as the laser wavelength decreases. This increase can be explained by the

increased absorption of InSe at shorter wavelengths.[26]

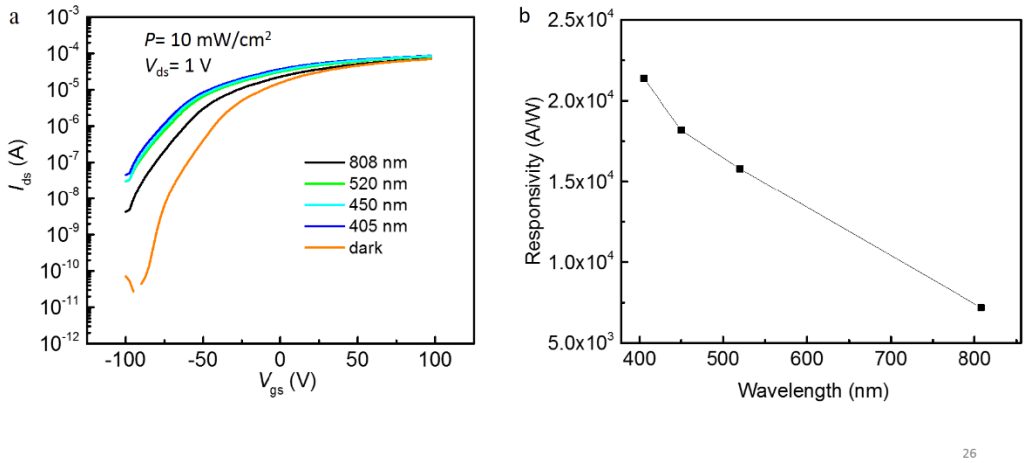

Figure S11. a) Transfer characteristics (I_{ds}–V_{gs}) of an InSe phototransistor (with channel thickness of 12 nm) in the dark and under illumination with a laser of wavelength λ = 808, 520, 450 and 405 nm and intensity of 10 mW/cm^2 at V_{ds} = 1 V. b) Responsivity as a function of λ at a gate bias of 0 V.

References

[1] S. Das, H. Y. Chen, A. V. Penumatcha, J. Appenzeller, *Nano Lett.* **2013**, 13, 100.

[2] G. Ghibaudo, *Phys. Status Solidi A* **1986**, 95, 323.

[3] G. Ghibaudo, *Electron Lett.* **1988**, 24(9), 543.

[4] C. Nguyenduc, S. Cristoloveanu, G. Ghibaudo, *Solid State Electron.* **1986**, 29, 1271.

[5] S. Y. Kim, S. Park, W. Choi, *Appl. Phys. Lett.* **2016**, 109, 152101.

[6] H. J. Chuang, X. Tan, N. J. Ghimire, M. M. Perera, B. Chamlagain, M. M. Cheng, J. Yan, D. Mandrus, D. Tomanek, Z. Zhou, *Nano Lett.* **2014**, 14, 3594.

[7] L. G. Kolla, S. Bhattacharjee, M. S, N. Bhat, *IEEE Electron Dev. Lett.* **2016**, 37, 797.

[8] Na, M. Shin, M.-K. Joo, J. Huh, Y. Jeong Kim, H. Jong Choi, J. Hyung Shim, G.-T. Kim, *Appl. Phys. Lett.* **2014**, 104, 233502.

[9] H. Y. Chang, W. Zhu, D. Akinwande, *Appl. Phys. Lett.* **2014**, 104, 113504.

[10] T. Y. Kim, M. Amani, G. H. Ahn, Y. Song, A. Javey, S. Chung, T. Lee, *ACS Nano* **2016**, 10, 2819.

[11] P. Bolshakov, P. Zhao, A. Azcatl, P. K. Hurley, R. M. Wallace, C. D. Young, *Appl. Phys. Lett.* **2017**, 111, 032110.

[12] H. A. Lee, S. Y. Kim, J. Kim, W. Choi, *J. Phys. D* **2017**, 50, 094001.

[13] J. Y. Park, H. E. Joe, H. S. Yoon, S. Yoo, T. Kim, K. Kang, B. K. Min, S. C. Jun, *ACS Appl. Mater. Interfaces* **2017**, 9, 26325.

[14] L. Valdez-Sandoval, E. Ramirez-Garcia, D. Jimenez, A. Pacheco-Sanchez, *Semicond. Sci. Technol.* **2020**, 35, 125016.

[15] B. C. Lee, C. M. Kim, H. K. Jang, J. W. Lee, M.-K. Joo, G.-T. Kim, *Appl. Surf. Sci.* **2017**, 419, 637.

[16] Y. Wang, J. Zhang, G. Liang, Y. Shi, Y. Zhang, Z. R. Kudrynskyi, Z. D. Kovalyuk, A. Patanè, Q. Xin, A. Song, *Appl. Phys. Lett.* **2019**, 115, 033502.

[17] M. Li, C. Y. Lin, S. H. Yang, Y. M. Chang, J. K. Chang, F. S. Yang, C. Zhong, W. B. Jian, C. H. Lien, C. H. Ho, H. J. Liu, R. Huang, W. Li, Y. F. Lin, J. Chu, *Adv. Mater.* **2018**, 30, e1803690.

[18] R. Baek, C. Baek, S. Jung, Y. Y. Yeoh, D. Kim, J. Lee, D. M. Kim, Y. Jeong, *IEEE T. Nanotech.* **2010**, 9, 212-217.

[19] N. Seong, T. Kim, H. Kim, T. J. Ha, Y. Hong, *Curr. Appl. Phys.* **2015**, 15, S8-S11.

[20] F. M. Huang, A. Liu, H. H. Zhu, Y. Xu, F. Balestra, G. Ghibaudo, Y. Y. Noh, J. Chu, W. W. Li, *IEEE Electron Dev. Lett.* **2019**, 40, 605.

[21] Y. Xu, T. Minari, K. Tsukagoshi, J. A. Chroboczek1, G. Ghibaudo, *J. Phys. D* **2010**, 107, 114507.

[22] W. Feng, F. Qin, M. Yu, F. Gao, M. Dai, Y. Hu, L. Wang, J. Hou, B. Li, P. Hu, *ACS Appl. Mater. Interfaces* **2019**, 11, 18511-18516.

[23] Y. Wang, J. Zhang, G. Liang, Y. Shi, Y. Zhang, Z. R. Kudrynskyi, Z. D. Kovalyuk, A. Patanè, Q. Xin, A. Song, *Appl. Phys. Lett.* **2019**, 115, 033502.

[24] Y. T. Huang, Y. H. Chen, Y. J. Ho, S. W. Huang, Y. R. Chang, K. Watanabe, T. Taniguchi, H. C. Chiu, C. T. Liang, R. Sankar, F. C. Chou, C. W. Chen, W. H. Wang, *ACS Appl. Mater. Interfaces* **2018**, 10, 33450.

[25] W. Feng, J.-B. Wu, X. Li, W. Zheng, X. Zhou, K. Xiao, W. Cao, B. Yang, J.-C. Idrobo, L. Basile, W. Tian, P. Tan, P. Hu, *J. Mater. Chem. C* **2015**, 3, 7022.

[26] M. Dai, H. Chen, R. Feng, W. Feng, Y. Hu, H. Yang, G. Liu, X. Chen, J. Zhang, C. Y. Xu, P. Hu, *ACS Nano* **2018**, 12, 8739.